


The zinc-finger protein OEF-1 stabilizes histone modification patterns and promotes efficient splicing in the *Caenorhabditis elegans* germline

Catherine E. McManus,¹ Mariateresa Mazzetto,¹ Guifeng Wei ,² Mei Han,¹ and Valerie Reinke^{1,*}

¹Department of Genetics, Yale University School of Medicine, New Haven, CT 06520, USA and

²Developmental Epigenetics, Department of Biochemistry, University of Oxford, Oxford OX1 3QU, UK

*Corresponding author: 333 Cedar St, NSB 386, New Haven, CT 06520, USA. Email: valerie.reinke@yale.edu

Abstract

To ensure stable transmission of genetic information to the next generation, germ cells frequently silence sex chromosomes, as well as autosomal loci that promote inappropriate differentiation programs. In *Caenorhabditis elegans*, silenced and active genomic domains are established in germ cells by the histone modification complexes MES-2/3/6 and MES-4, which promote silent and active chromatin states, respectively. These states are generally mutually exclusive and modulation of one state influences the pattern of the other. Here, we identify the zinc-finger protein OEF-1 as a novel modifier of this epigenetic balance in the *C. elegans* germline. Loss of *oef-1* genetically enhances *mes* mutant phenotypes. Moreover, OEF-1 binding correlates with the active modification H3K36me3 and sustains H3K36me3 levels in the absence of MES-4 activity. OEF-1 also promotes efficient mRNA splicing activity, a process that is influenced by H3K36me3 levels. Finally, OEF-1 limits deposition of the silencing modification H3K27me3 on the X chromosome and at repressed autosomal loci. We propose that OEF-1 might act as an intermediary to mediate the downstream effects of H3K36me3 that promote transcript integrity, and indirectly affect gene silencing as a consequence.

Keywords: germ cells; chromatin; splicing; X chromosome; *C. elegans*

Introduction

Germ cells require a precise balance between gene expression and repression that largely depends upon the establishment of distinct chromatin states across the genome. Two important histone modifications contribute to the formation of these states: H3K27me3 marks repressive domains, where it limits chromatin accessibility to transcriptional regulators (van Mierlo et al. 2019), while H3K36me3 is present at transcribed genes, where it suppresses cryptic transcription initiation and promotes mRNA splicing, RNA processing, and DNA repair (Meers et al. 2017; Li et al. 2019). In *Caenorhabditis elegans*, these modifications are established via the chromatin-modifying pathway consisting of the histone methyltransferase (HMT) MES-4 and the Polycomb Repressive Complex 2 (PRC2) orthologs MES-2/3/6 (Bender et al. 2004, 2006; Gaydos et al. 2012). MES-4 promotes H3K36me3 accumulation on autosomes, which leads to concentration of H3K27me3 on the X by MES-2/3/6 (Gaydos et al. 2012). Loss of MES activity results in inappropriate activation of X-linked genes and second-generation sterility (Capowski et al. 1991; Bender et al. 2006). The two marks occupy mutually exclusive domains of the genome (Gaydos et al. 2012; Evans et al. 2016), leading to a model in which the presence of one modification prevents the accumulation of the other at specific loci. However, beyond the core methyltransferase complexes, few

factors that might influence this relationship between H3K27me3 and H3K36me3 have been identified.

We previously characterized the zinc-finger protein OEF-1 (Oocyte-Excluded Factor 1) as a novel, germline-specific nuclear factor that is required for a normal rate of progression through germ cell development (McManus and Reinke 2018). Germ cells lacking OEF-1 activity display precocious proliferation, an activated synaptic checkpoint, and more rapid progression through differentiation (McManus and Reinke 2018). However, the molecular activity of OEF-1 that might underlie these phenotypes is unknown. We previously demonstrated that OEF-1 is nuclear and preferentially associates with autosomal genes expressed in the germline in a distinctive distributed pattern across gene bodies. Indeed, the low, broad profile of OEF-1 binding can be seen on most germline-expressed genes, even for those that do not reach statistical significance in peak-calling methods. This observation suggests that OEF-1 might directly affect transcript levels of the genes at which it is located. Alternatively, OEF-1 might have a chromatin-associated function that indirectly affects downstream germline processes through another mechanism. Here, we set out to distinguish between these possibilities.

We first determine that OEF-1 has minimal effect on transcript abundance in germ cells, with mild reduction of X-linked transcript abundance. Consistent with this observation, loss of

Received: April 12, 2021. Accepted: September 7, 2021

© The Author(s) 2021. Published by Oxford University Press on behalf of Genetics Society of America.

This is an Open Access article distributed under the terms of the Creative Commons Attribution License (<https://creativecommons.org/licenses/by/4.0/>), which permits unrestricted reuse, distribution, and reproduction in any medium, provided the original work is properly cited.

OEF-1 increases the silencing mark H3K27me3 throughout the genome, particularly on the X chromosome. However, OEF-1 binding primarily correlates with the presence of the activating histone modification H3K36me3, and OEF-1 is necessary to prevent H3K36me3 levels from decreasing in *mes-4* mutants. Moreover, loss of OEF-1 activity results in reduced splicing efficiency of germline-expressed mRNAs. These observations together suggest that OEF-1 might assess or interpret H3K36me3 levels to mediate downstream functions such as splicing that are associated with productive gene expression. We hypothesize that this activity would indirectly affect gene repression by disrupting the balance between activating and silencing modifications.

Materials and methods

Caenorhabditis elegans strains

Strains used in this study are listed in Supplementary Table S7. Strains were maintained by standard methods on NGM plates seeded with OP50 bacteria as described (Brenner 1974). Bristol N2 was used as the wild-type reference strain. All growth was performed at 20°C, except for *glp-4* strains which were maintained at 15°C and shifted to 25°C before collection. For balanced strains, larval stage 4 (L4) worms expressing pharynx GFP were picked to ensure the selection of first-generation homozygotes in downstream assays.

Brood size analyses

L4 worms were singly placed on seeded plates and moved to fresh plates each day until embryo production ceased. Unhatched embryos were scored as dead 24 h after the mother was removed. Live larvae were counted two days later. To score the presence or absence of germlines, L4s were aged 8–9 h before fixation in 20 μ l of Carnoy's fix (300 μ l 100% ethanol, 150 μ l chloroform, and 50 μ l acetic acid) on Super Frost slides. Twelve microliters of 1 ng/mL DAPI diluted in M9 was added to coverslips, which were touched to slides and sealed with nail polish before scoring.

Immunostaining

Adults 16–20 h post-L4 were dissected to release gonads in 1.1x egg salts (10X egg salts: 250 mM HEPES pH 7.4, 1.18 M NaCl, 20 mM MgCl₂, 20 mM CaCl₂, 4.8 mM KCl) with 0.1% Tween 20 and 0.3 mM levamisole. Gonads were fixed with 1% formaldehyde, then freeze-cracked on a metal block embedded in dry ice and immediately placed in –20°C methanol. Blocking was performed using 0.5% BSA in PBST for 30 min at room temperature. For histone modification staining, the area around the gonads was dried with a Kim wipe and a circle was drawn around the tissue using a mini PAP pen before the addition of the primary antibody. Primary and secondary antibody incubations were performed overnight at 4°C in a 50 μ l volume. The following antibody dilutions were used: 1:50 anti-OEF-1 (McManus and Reinke 2018); 1:2000 anti-GFP (Abcam ab13970); 1:20 anti-H3K4me2 (EMD Millipore CMA303); 1:200 anti-H3K27me3 (EMD Millipore 07-449); 1:1000 anti-H3K36me3 (Abcam ab9050). Secondary antibodies (Molecular Probes) were diluted 1:500. Slides were mounted in Vectashield anti-fade mounting medium (Vector Laboratories) with no. 2 coverslips (Corning) and sealed with nail polish. 0.375 μ m Z stacks were acquired using a Zeiss Axioplan microscope with a 20X, 40X, or 100X objective, and a Zeiss AxioCam MRm camera, and processed using Axiovision software.

For H3K27me3 mean intensity measurements, ImageJ (NIH) was used to make Z projection images. The X chromosome was identified in germ cells by lack of H3K4me2 staining and

enrichment for H3K27me3 staining. In each germ cell in which a clear X chromosome could be identified, a representative autosome was identified by high levels of H3K4me2 and low levels of H3K27me3. The free draw tool was used to outline a representative X and a representative autosome in wild-type and *oef-1(vr25)* germ cells. The mean intensity of H3K27me3 in the outlined areas was recorded. The measurements were repeated for 6–8 nuclei per gonad, 7 gonads per genotype (46–48 nuclei total).

For the H3K36me3 proliferative zone reduction phenotype, extruded and well-stained gonads were scored as having no reduction, slight reduction, or strong reduction in H3K36me3 staining in the proliferative zone as compared to pachytene in the same gonad. The genotypes of the slides were blinded before scoring. The slides represented two or three independent staining experiments all scored in the same sitting.

Germ nuclei isolation

Germ nuclei isolation was performed as in Han et al. (2019). N2 and *oef-1(vr25)* worms were grown to gravid on NGM plates, bleached, and hatched overnight in M9 for at least 24 h. Fifty thousand L1s were plated on enriched plates and grown until most worms had ≥ 4 embryos. Around 1 million worms were used per nuclei collection. The worms were washed off with M9 in sets of 6 plates into 50 mL falcon tubes, washed twice with M9, then were fixed for 28 min in 2% formaldehyde diluted in M9. After a wash with 1 M Tris (pH 7.5), the worms were washed twice more with M9. The worms were then washed with chilled Nuclei Purification Buffer (NPB) (50 mM HEPES pH 7.5, 40 mM NaCl, 90 mM KCl, 2 mM EDTA, 0.5 mM EGTA, 0.1% Tween 20, 0.2 mM DTT, 0.5 mM PMSF, 0.5 mM spermidine, 0.25 mM spermine, and proteinase inhibitor cocktail—1 tablet per 25 mL NPB).

The fixed and washed worms were resuspended in NPB and transferred to prechilled 7 mL glass Dounce homogenizers (Wheaton). One Dounce homogenizer was used per set of 6 plates. Fifteen loose strokes were followed by 30 tight strokes with a quarter turn between each Dounce. The worms were transferred into chilled 50 mL falcon tubes, and NPB was added to 30 mL. The falcon tubes were vortexed on medium-high speed for 30 s, followed by 15 min on ice. The vortex and ice incubation were repeated. The worms were then passed through three 40 μ m filters (Fisherbrand) followed by eight 20 μ m filters (pluriSelect). The nuclei were spun at 3100 rpm for 6 min at 4°C. The supernatant was removed, and the nuclei were resuspended in 1 mL NPB and transferred to a nonstick 1.5 mL tube (Ambion). A 5 μ l sample of nuclei was removed, incubated with DAPI, and counted using a hemacytometer (Hausser Scientific). Finally, the nuclei were spun at 4°C at 4000 rpm for 5 min, the supernatant was removed, and the nuclei were flash frozen in liquid nitrogen. The nuclei were stored at –80°C until sonication. 2–3 nuclei collections were pooled per ChIP experiment (for a total of 15–20 million nuclei per IP).

ChIP-seq

Isolated germ cell nuclei were thawed on ice, and 120 μ l of Nuclear Lysis Buffer (50 mM Tris pH 8.0, 10 mM EDTA, 1% SDS, 0.5 mM PMSF, proteinase inhibitor cocktail) was added to each sample. The nuclei were vortexed vigorously for 1 min followed by 1 min on ice. The vortex step was repeated. The nuclei were sonicated at 2°C in a water bath sonicator (Misonix S-4000) at 20% amplitude, with 10 s on/10 s off pulses for a total process time of 20 min.

1.2 mL of FA buffer (50 mM HEPES pH 7.5, 1 mM EDTA, 1% Triton X-100, 0.1% sodium deoxycholate, 150 mM NaCl, 1 mM

DTT, 0.5 mM PMSF, proteinase inhibitor cocktail) was added to each sonicated sample. A 1:20 volume of 20% sarkosyl was added, and the samples were spun at $13,000 \times g$ for 5 min at 4°C . The supernatant was transferred to a new tube, and then 5% of the lysate was removed for the input sample. The input samples were stored at -20°C overnight. Five micrograms of anti-H3K27me3 (Active Motif MAB10323) or anti-H3K36me3 (Active Motif MAB10333) was incubated with each IP sample overnight at 4°C with rotation.

The next day, the input samples were thawed on ice and were incubated with $2 \mu\text{l}$ of 10 mg/mL RNase A for 2 h at room temperature. Approximately $40 \mu\text{l}$ of Protein G Sepharose beads (GE Healthcare) were washed 4 times with 1 mL FA, spinning for 2 min at $2500 \times g$ between each wash. The entire IP sample was added directly to the beads, and the samples were rotated for 2 h at 4°C .

After the RNase A treatment of the input samples, $230 \mu\text{l}$ of elution buffer (1% SDS in TE, 250 mM NaCl) was added to each input sample to bring the total volume up to $300 \mu\text{l}$. $2.05 \mu\text{l}$ of 19.5 mg/mL proteinase K was added, and the input samples were incubated at 55°C for 3 h.

After the 2-h bead incubation, the beads were washed at room temperature as follows (1 mL for each wash): 2 times with FA for 5 min each, 1 time with FA with 500 mM NaCl for 10 min, 1 time with TEL (0.25 M LiCl, 1% NP40, 1% sodium deoxycholate, 1 mM EDTA, 10 mM Tris pH 8.0) for 10 min, 2 times with TE for 5 min each. One hundred and fifty microliter of elution buffer was added to each sample and was incubated at 65°C for 15 min with occasional vortexing. The elution step was repeated and the eluates were pooled. $1.03 \mu\text{l}$ of 19.5 mg/mL proteinase K was added to the eluates and the incubation was performed at 55°C for 1 h. After the proteinase K digestion, input and IP samples were incubated overnight at 65°C to reverse the crosslinks. The next day, input and ChIP DNA were purified using the QIAquick PCR Purification Kit. Samples were eluted in $40 \mu\text{l}$ TE and submitted for library preparation and sequencing at the Yale Center for Genome Analysis.

Somatic samples were prepared as described (Kudron et al. 2018). *glp-4* and *glp-4; oef-1* animals were grown at the permissive temperature of 15°C and embryos were isolated by bleaching and hatching overnight in M9 at 15°C . Forty thousand L1s were plated on peptone-enriched plates and were grown at 25°C until the young adult stage. Adult worms were washed off plates with M9 and were washed 3 times, spinning at $3100 \times g$ between each wash. Worms were fixed in 50 mL 2% formaldehyde in M9 for 28 min at room temperature. After spinning, worms were washed with 50 mL 1 M Tris, pH 7.5 followed by two more washes with M9. A final wash with FA buffer was performed before pellets were flash-frozen and stored at -80°C . After thawing on ice, pellets were resuspended in $750 \mu\text{l}$ FA buffer and transferred to a 2 mL Kontes dounce (Kimble Chase). Samples were dounced 15 times for two cycles with the A pestle and 15 times with the B pestle for four cycles with a 1 min hold between each cycle. Pellets were sonicated using a SFX250 sonifier (Branson) in 1.5 mL FA buffer in an ice bath at 22% amplitude with 10 s on/1 min off pulses for a total process time of 5 min 40 s. Sonicated samples were transferred to nonstick tubes and spun at $13,000 \times g$ for 15 min at 4°C . 4.4 mg of lysate was used per IP in a volume of $400 \mu\text{l}$. 1:20 volume of 20% Sarkosyl solution was added to each $400 \mu\text{l}$ sample and the samples were spun at $13,000 \times g$ for 5 min at 4°C . The supernatant was transferred to new nonstick tubes. The rest of the ChIP protocol was performed as for isolated germ nuclei.

Sequencing and data analysis

Seventy-five-bp single-end reads were sequenced on an Illumina HiSeq2500 in rapid-run mode. The raw ChIP and corresponding input fastq sequencing reads were mapped to the genome (version ce10) by Bowtie2 (v2.3.2) (Langmead and Salzberg 2012) with default parameters. The datasets for two replicates were merged for further analysis. To eliminate the replicate bias, the alignment file (bam) from the sample with larger library size was downsampled to the size of the replicate with smaller library size, and then merged together by Samtools (v1.3) (Li et al. 2009). Peaks were called by MACS2 (v2.1.1) (Zhang et al. 2008) with the key parameter (-q 0.001 -nomodel -extsize 200) against the merged input. Normalization was performed by bamCompare, which scales the IP to input using read number, and wig files were generated using a custom script (<https://github.com/guifengwei/glib/blob/master/bam2wig.py>), which also scales IP to input using read number. Heatmaps were generated by ngs.plot.r (v2.63) (Shen et al. 2014) with the default parameters except (-G ce10 -R genebody -SC global). Genes longer than 1 kb were kept for analysis. The germline-enriched genes were defined as in (Han et al. 2019). Metagene plots were generated by computing matrices binned into 50 bp windows for histone modifications or 100 bp windows for OEF-1 using computeMatrix v2.5.0 and plotProfile v2.5.0 in deepTools (Ramírez et al. 2016). The correlation plot was generated using multiBigwigSummary followed by plotCorrelation in deepTools. The genomic regions used were all genes including 2 kb up/downstream of the TSS/TES. Supplementary Table S8 lists all samples used for genomic analyses.

RNA-sequencing

N2 and *oef-1(vr25)* worms were grown to gravid on large NGM plates, bleached, and hatched overnight in M9 in the absence of food. The next day, 200 L1s were plated on small NGM plates and were grown to young adulthood. One hundred young adults of each genotype were dissected to release gonads in M9 with 0.1% levamisole and 0.1% Tween 20, cut at the spermatheca, and transferred in as little liquid as possible to $100 \mu\text{l}$ of TRIzol (Invitrogen) on ice. The samples in TRIzol were flash frozen in liquid nitrogen and were stored at -80°C until subsequent purification steps. Growths and dissections were repeated for a total of 400 gonads per replicate for each genotype.

Samples were thawed in a 37°C water bath, vortexed, and flash frozen again in liquid nitrogen. The freeze-thaw step was repeated twice more. Hundred microliters of chloroform was added, the samples were shaken for 15 s, and then left to sit for 8 min at room temperature. Samples were spun at $12,000 \times g$ for 20 min at 4°C . The top aqueous layer was removed to a fresh tube, then an equal volume of isopropanol was added and incubated at -20°C overnight. The next day, the samples were spun at $12,000 \times g$ for 30 min at 4°C . The supernatant was discarded, and the pellets were washed with $500 \mu\text{l}$ of 75% ethanol and spun at full speed at 4°C for 5 min. The wash and spin steps were repeated. As much ethanol was removed as possible, and the pellets were dried for 5 min. Finally, the pellets were resuspended with $20 \mu\text{l}$ of RNase-free water preheated to 55°C . DNase treatment was performed using the Ambion DNA-free kit according to the manufacturer's instructions. DNase-treated samples were then cleaned up using the RNeasy Mini Kit and eluted in $50 \mu\text{l}$ of RNase-free water.

Ribozero library preparation was performed at the Yale Center for Genome Analysis. Seventy-five bp paired-end reads were

sequenced on an Illumina HiSeq2500. Trimmed reads were mapped to WS220 using TopHat v2.0.14 (Trapnell et al. 2012; Kim et al. 2013) and assembled using Cufflinks v2.2.1 and Cuffmerge v1.1.4 (Trapnell et al. 2010). Differential expression testing between N2 and *oef-1(vr25)* assemblies was performed using CuffDiff v2.2.1 (Trapnell et al. 2013) and DESeq2 (Love et al. 2014).

For the intron retention analysis, RNA-seq paired-end reads were aligned to ce10 reference genome using HISAT2 (Kim et al. 2019) with default parameters. Reads were then assembled using two independent methods: IntERESt package (Oghabian et al. 2018) and Rsubread (Liao et al. 2019). Both were used to count intron and splice junction reads, using minOverlap of 60 bp for the latter. Intron retention differential analysis was performed using DESeq2 (Anders and Huber 2010) with default parameters and a multi-factor design (condition + exon-intron): the samples from the “control” dataset were mixed and a correction for batch effect was applied. Visualization of results and generally applicable gene enrichment (GAGE) analysis were performed using ggplot2 (Wickham 2016) and gage (Luo et al. 2009) packages on Bioconductor. RNA degradation was measured by a calculation of “transcript integrity”, which determines the frequency of defined ends of transcripts compared to shortened or incomplete transcripts, using RseQC software for Linux (Wang et al. 2016). Supplementary Table S8 lists all samples used for genomic analyses.

Results

Loss of OEF-1 activity has minor effects on germline gene expression

In order to gain more insight into the function of OEF-1 in the germline, we first determined whether loss of *oef-1* results in significant changes in transcript abundance in gonads. We used the previously defined *oef-1(vr25)* allele, which contains a 56-bp frameshift deletion in exon 2 generated by CRISPR/Cas9 gene editing (McManus and Reinke 2018). We initially used CuffDiff to perform differential expression analysis of three replicates of RNA-sequencing of dissected adult gonads from wild-type and *oef-1(vr25)* mutants and found relatively few significant changes in gene expression (Figure 1A). We therefore also applied DESeq2 to determine whether this result was consistent regardless of computational approach. Again, we saw few transcripts that were reproducibly and significantly up- or downregulated in all three replicates of RNA-seq (Figure 1B). Comparison between the two analyses identified only 37 genes with significantly different expression identified by both programs, and these genes exhibited no obvious similarities in chromosomal location, gene function, or expression patterns (Supplementary File S1). Moreover, of the 37 genes, only 12 are directly bound by OEF-1 (Supplementary File S1). Together, these analyses indicate that OEF-1 does not have a consistent, significant effect on transcript abundance of the vast majority of its autosomal target genes. However, although few individual X-linked genes exhibited statistically significant changes in gene expression, we found a subtle yet global decrease in X chromosome gene expression in *oef-1(vr25)* compared to wild type that was not detected for autosomes using either the CuffDiff or DESeq2 datasets (Figure 1, C and D). This result suggests that X-linked transcripts, which are already present at very low levels in germ cells (Kelly et al. 2002), are further reduced upon loss of OEF-1.

oef-1 mutant germ nuclei exhibit increased enrichment of H3K27me3 on the X chromosome

The effect on X chromosome gene expression was surprising because OEF-1 has little binding on the X (McManus and Reinke 2018). Given the established importance of H3K27me3 on X chromosome silencing (Gaydos et al. 2012), we wondered whether OEF-1 might affect H3K27me3 levels. We first performed immunostaining to monitor H3K27me3 in germ nuclei, and specifically observed detectable enrichment of H3K27me3 on the X chromosome relative to the autosomes as demonstrated previously (Gaydos et al. 2012). Strikingly, H3K27me3 staining of the X appeared even stronger in *oef-1(vr25)* mutant germ cells compared to wild type (Figure 2A). Quantification of the signal indeed detected a significant increase in the average mean H3K27me3 intensity for *oef-1(vr25)* X chromosomes compared to wild type (Figure 2B). On the other hand, there was no significant difference in the mean intensities of H3K27me3 staining between *oef-1(vr25)* and wild-type autosomes (Figure 2B). This result suggests that loss of OEF-1 leads to further enrichment of H3K27me3 on the X chromosome and is consistent with increased downregulation of X-linked gene expression in *oef-1* mutants.

H3K27me3 accumulation increases genome-wide in *oef-1* mutant germ nuclei

In order to investigate the changes in H3K27me3 accumulation in *oef-1* mutants at the resolution of individual loci, we used a method to isolate germ nuclei (Han et al. 2019) from wild type and *oef-1(vr25)* adults, and then performed H3K27me3 chromatin immunoprecipitation followed by sequencing (ChIP-seq). As a soma-only control, we also performed H3K27me3 ChIP-seq on *glp-4(bn2)* and *glp-4; oef-1* whole animals, which lack germ cells at the restrictive temperature of 25°C (Beanan and Strome 1992). Because this isolation method was recently developed, we first confirmed that the wild-type H3K27me3 chromatin profiles accurately reflect expected germline and somatic patterns. Previous studies demonstrate that the X chromosome is enriched for H3K27me3 relative to autosomes in germ nuclei, and that any genes marked by H3K27me3, whether on the X or on autosomes, are likely to have very low expression levels in wild-type adult germ cells (Kelly et al. 2002; Reinke et al. 2004). We therefore first examined the H3K27me3 profile across all chromosomes and found that H3K27me3 is more broadly and evenly distributed across the X relative to autosomes in germ nuclei but not in the soma (Supplementary Figure S1A). In addition, the genes with enriched expression in the germline have relatively low H3K27me3 signal in isolated germ nuclei compared to genes with enriched expression in the soma (Supplementary Figure S1B). In particular, genes primarily expressed in meiotic or oogenic germ cells exhibit very low levels of H3K27me3 (Supplementary Figure S1C). Thus, these datasets accurately represent the known germline- and soma-specific patterns of H3K27me3.

We next compared H3K27me3 accumulation patterns between wild type and *oef-1(vr25)* isolated germ nuclei and found elevated average levels of H3K27me3 on X-linked genes in *oef-1(vr25)* (Figure 3A, Supplementary Figure S2), which we confirmed by metagene and heatmap analysis (Figure 3B, Supplementary Figures S3–S6). Notably, the pattern of H3K27me3 accumulation in *oef-1* germ nuclei does not appear to spread or expand beyond wild-type regions (Figure 3A, Supplementary Figures S3–S6). The somatic datasets showed no change in average H3K27me3 levels on the X chromosome, which was expected given that OEF-1 expression is limited to germ cells (McManus

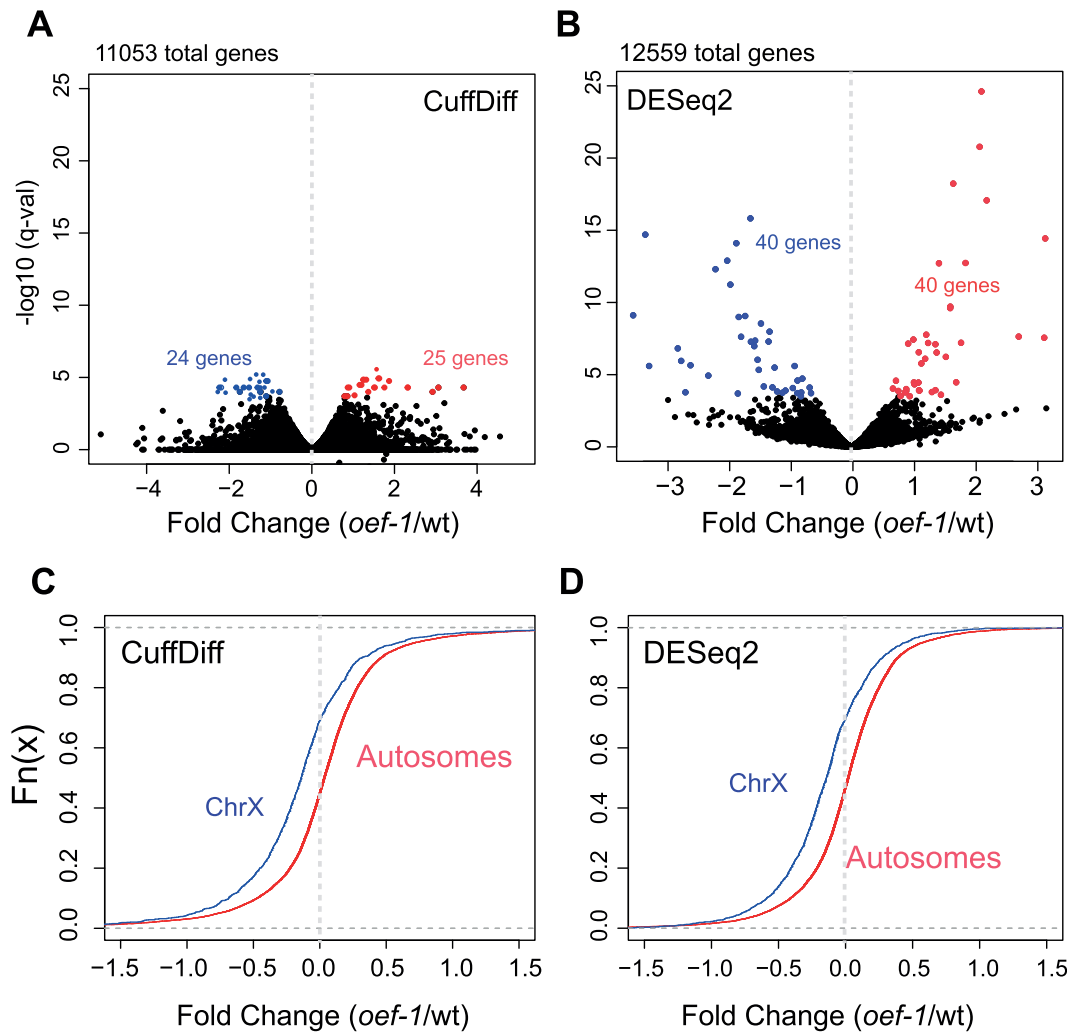


Figure 1 *oef-1* mutants display few changes in transcript abundance but a global decrease in X-linked expression. (A,B) Volcano plots showing fold change of gene expression in *oef-1(vr25)* mutants (x-axis) compared to wild type relative to \log_{10} of q -value (y-axis) using either CuffDiff (A) or DESeq2 (B) programs. Blue dots show significantly downregulated genes, and red indicates significantly upregulated; cases with q -value < 0.05 (CuffDiff) and $p_{adj} < 0.05$ (DESeq2) were counted as significant. Data are from the combined analysis of three biological replicates. (C, D) Cumulative plot showing the distribution of gene expression changes for X-linked (blue) and autosomal (red) transcripts in *oef-1(vr25)* dissected gonads relative to wild-type from the CuffDiff analysis (C, $N = 1921$ X-linked genes, 12,270 autosomal genes) and DESeq2 analysis (D, $N = 1565$ X-linked genes, 10,994 autosomal genes). Only genes with a \log_2 change of less than 1.5-fold or more than -1.5 -fold are shown. Data are from the combined analysis of three biological replicates. $P < 2.2 \times 10^{-16}$, Wilcoxon test.

and Reinke 2018) (Figure 3, A and B, Supplementary Figures S2–S6). These data are consistent with increased H3K27me3 accumulating on the X chromosome in germ but not somatic nuclei upon loss of OEF-1.

Notably, we also identified 485 autosomal genes with a greater than twofold increase in H3K27me3 levels in *oef-1(vr25)* mutant germ cells (Figure 3B, Supplementary Figure S5). This increase was likely not detectable by immunofluorescence (Figure 2B) because these genes are dispersed across the five autosomes. Of the 485 autosomal genes with higher H3K27me3 in *oef-1(vr25)* germ nuclei (Supplementary Table S1, Supplementary File S2), 82% are expressed either during spermatogenesis in the L4 stage or in the soma (Ortiz et al. 2014) and are therefore likely expressed at low levels in the adult germline. Indeed, their expression is significantly lower than the average of all autosomal genes and more similar to X-linked genes (Figure 3C). These data support an indirect role for OEF-1 in limiting the levels of H3K27me3 on the X chromosome and at autosomal loci enriched for that modification.

Loss of OEF-1 has minimal effect on H3K36me3 levels in germ nuclei

Although OEF-1 affects H3K27me3 levels, OEF-1 is not localized to genomic regions harboring that modification but instead is present across gene bodies of most germline-expressed genes on autosomes (McManus and Reinke 2018), and therefore should be more closely associated with H3K36me3. Given the known balance between H3K27me3 and H3K36me3, we hypothesized that the change in H3K27me3 levels in *oef-1* mutants might occur as a response to changes in H3K36me3 levels. We therefore performed H3K36me3 ChIP-seq in isolated germ and somatic nuclei from wild type and *oef-1(vr25)* mutants. As before, we first confirmed that the wild-type H3K36me3 profile reflected the expected pattern for the germline and soma. Indeed, H3K36me3 levels were depleted from the X chromosome relative to autosomes in germ nuclei but not in the soma (Supplementary Figure S1A) (Gaydos et al. 2012). Moreover, H3K36me3 was enriched on genes known to be expressed in the germline at much greater levels than in the soma (Supplementary Figure S1, B and C). Finally, the

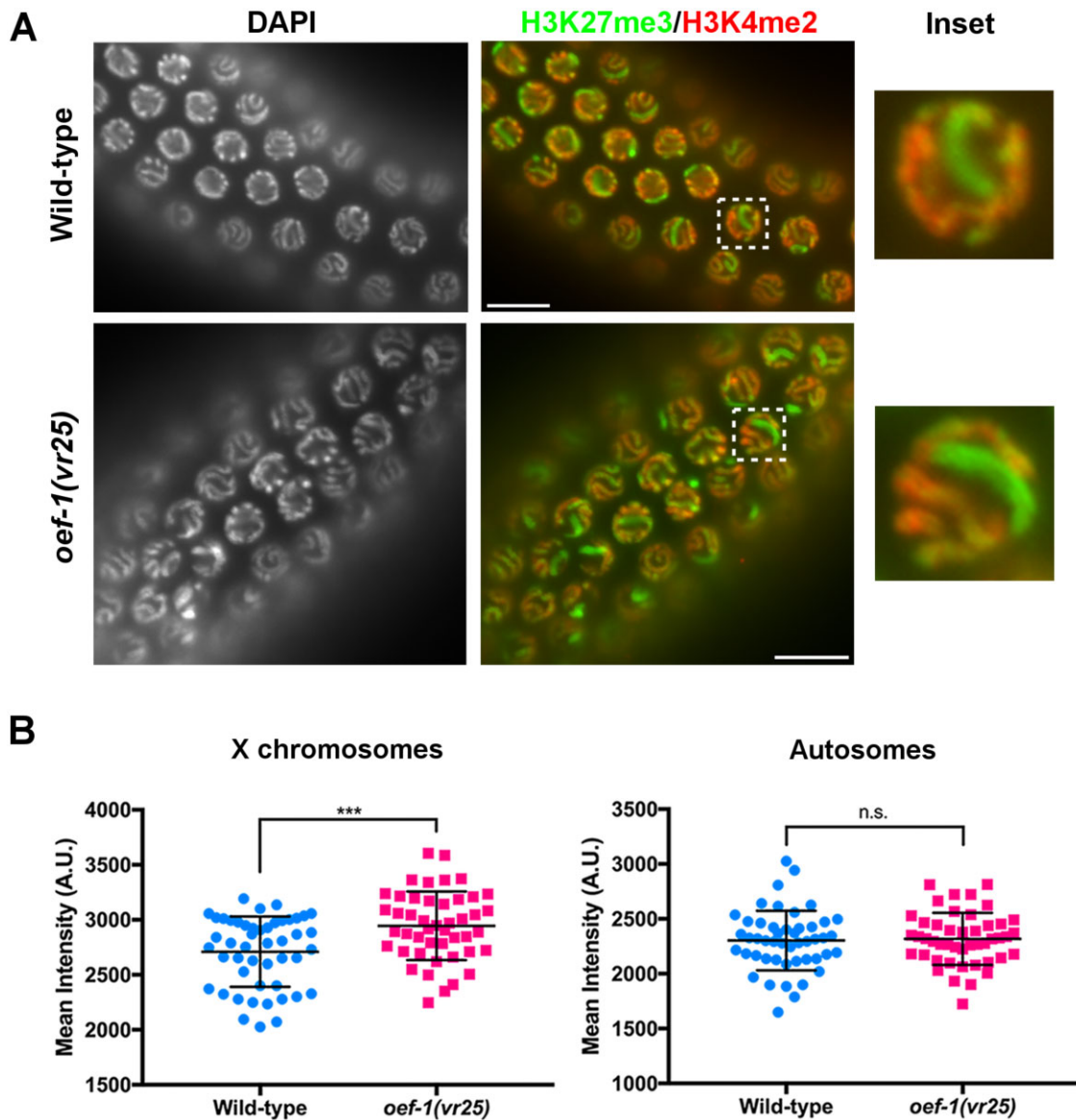


Figure 2 *oef-1* mutant germ cells exhibit higher enrichment of H3K27me3 on the X chromosome. (A) Representative wild-type and *oef-1(vr25)* pachytene nuclei co-stained with the X chromosome-enriched histone modification H3K27me3 (green) and the autosomal-specific histone modification H3K4me2 (Kelly et al. 2002) (red). DAPI (DNA) is at left. Box indicates inset at right. Scale bars, 10 μ m. (B) Quantification of H3K27me3 staining. The mean intensities of H3K27me3 staining for X chromosomes (left) were measured in wild-type (2710 A.U.) and *oef-1(vr25)* (2946 A.U.) pachytene nuclei. H3K27me3 intensity was equivalent between wild-type (2302 A.U.) and *oef-1(vr25)* (2318 A.U.) for representative autosomes (right). *** $P < 0.001$, unpaired t-test. n.s., not significant. A.U., arbitrary units. $n \geq 6$ nuclei from 7 gonads per genotype (≥ 46 nuclei total). Error bars represent S.D.

H3K36me3 and H3K27me3 profiles are anti-correlated in isolated germ nuclei and in somatic tissues (-0.58 and -0.62 , respectively, Pearson's correlation coefficient; Supplementary Figure S1, D and E). Thus, the germline and somatic H3K36me3 datasets replicate the expected patterns in each tissue.

We then examined the relationship between H3K36me3 levels and OEF-1 in wild-type germ nuclei. We found a strong positive genome-wide correlation between H3K36me3 and OEF-1 binding levels (0.7 , Pearson's correlation coefficient) (Figure 4A). The similarity in genomic profiles was also apparent across individual genes as viewed by genome browser (Supplementary Figure S7). We next determined whether loss of OEF-1 affected H3K36me3 levels. Visible differences in H3K36me3 abundance or pattern between wild type and *oef-1* mutants were not detected (Figure 4B). We therefore performed metagene analysis to try to identify more subtle differences (Figure 4C, Supplementary Figures S3–

S6), which confirmed that OEF-1 does not lead to a significant alteration of H3K36me3 patterns or abundance across gene bodies for either germline-expressed or X-linked genes. At the 5' and 3' end of genes, there is a slight dip in H3K36me3 levels in *oef-1* germ nuclei relative to wild type. Strikingly, the inverse pattern is seen in somatic nuclei, which do not express OEF-1 (Figure 4C, Supplementary Figures S4–S6). Whether the change in H3K36me3 levels at gene ends has biological significance is currently unclear. Overall, loss of OEF-1 activity alone does not measurably affect the distribution or steady-state level of H3K36me3 in germ cells.

OEF-1 acts redundantly with MES-4 to promote germline H3K36me3

The localization of OEF-1 to sites of H3K36me3 as well as the increased H3K27me3 levels in *oef-1* mutants suggested that OEF-1

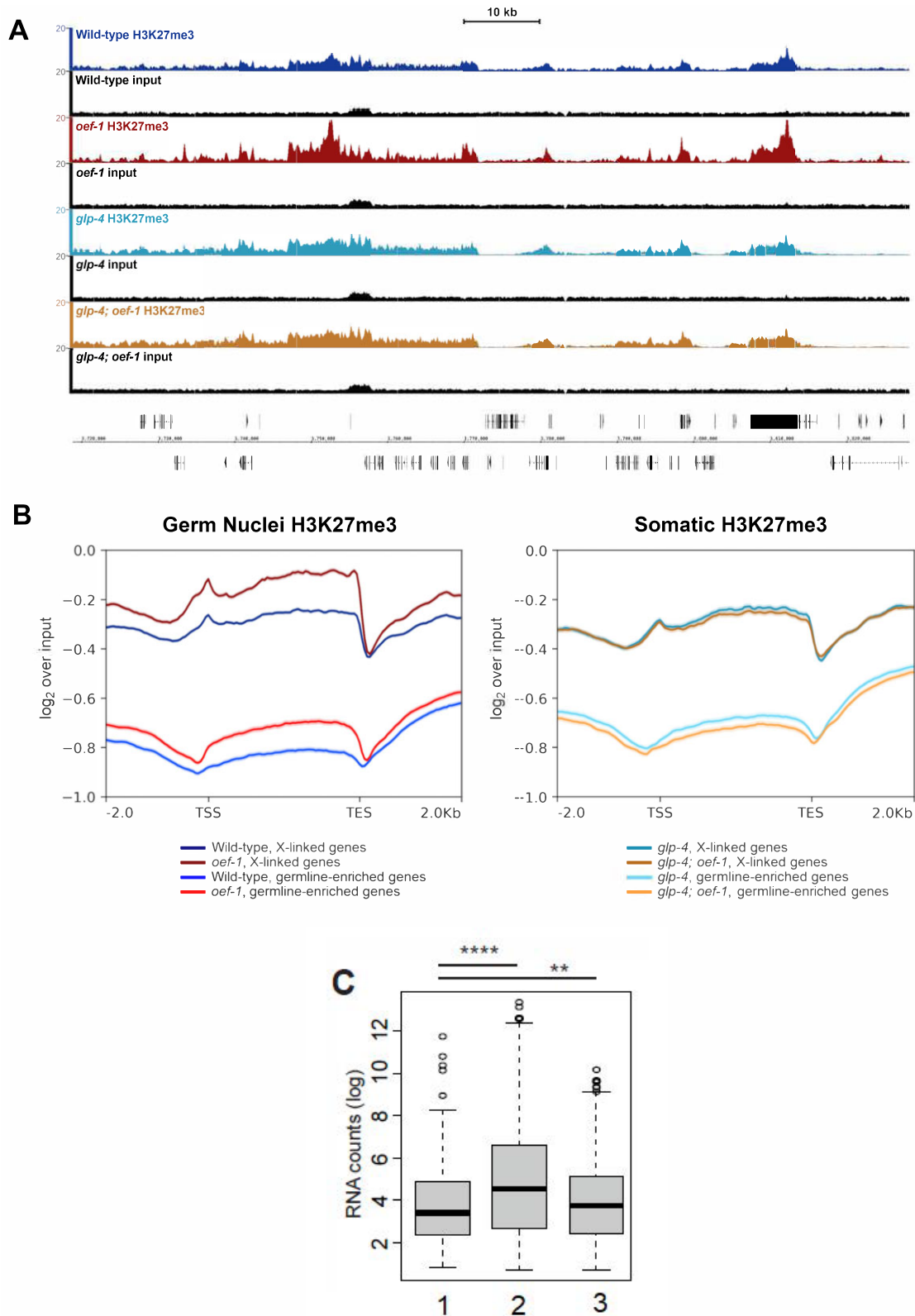


Figure 3 H3K27me3 accumulation increases genome-wide in *oef-1* mutant germ nuclei. (A) Browser view of H3K27me3 ChIP-seq on the X chromosome. Wild-type germ nuclei track is shown in navy, *oef-1* germ nuclei in maroon, *glp-4* soma in teal, *glp-4; oef-1* soma in dark orange. Input tracks in black are shown below each sample. Coordinates shown are chrX: 3,717,067–3,832,532. Scale bar, 10 kb. (B) Left: Metagene analysis of H3K27me3 ChIP-seq signal for wild-type (blue and navy) and *oef-1* (*vr25*) (red and maroon) isolated germ nuclei across either X-linked genes (maroon and navy) or germline-enriched autosomal genes (red and blue). ChIP-seq signal is \log_2 over input. Right: Metagene analysis of H3K27me3 ChIP-seq signal for *glp-4* (dark teal and light teal) and *glp-4; oef-1* (dark orange and light orange) somatic samples across either X-linked genes (dark teal, dark orange) or germline-enriched autosomal genes (light teal and light orange). TSS, transcription start site. TES, transcription end site. Shading indicates standard error. (C) Box plot showing significant difference in FPKM distribution for the 485 autosomal genes with increased H3K27me3 in *oef-1* mutants (“1”) compared to all autosomal genes (“2”) (**** $P < 2.2e-16$) and to all X-linked genes (“3”) (** $P = 0.004754$), Wilcoxon test.

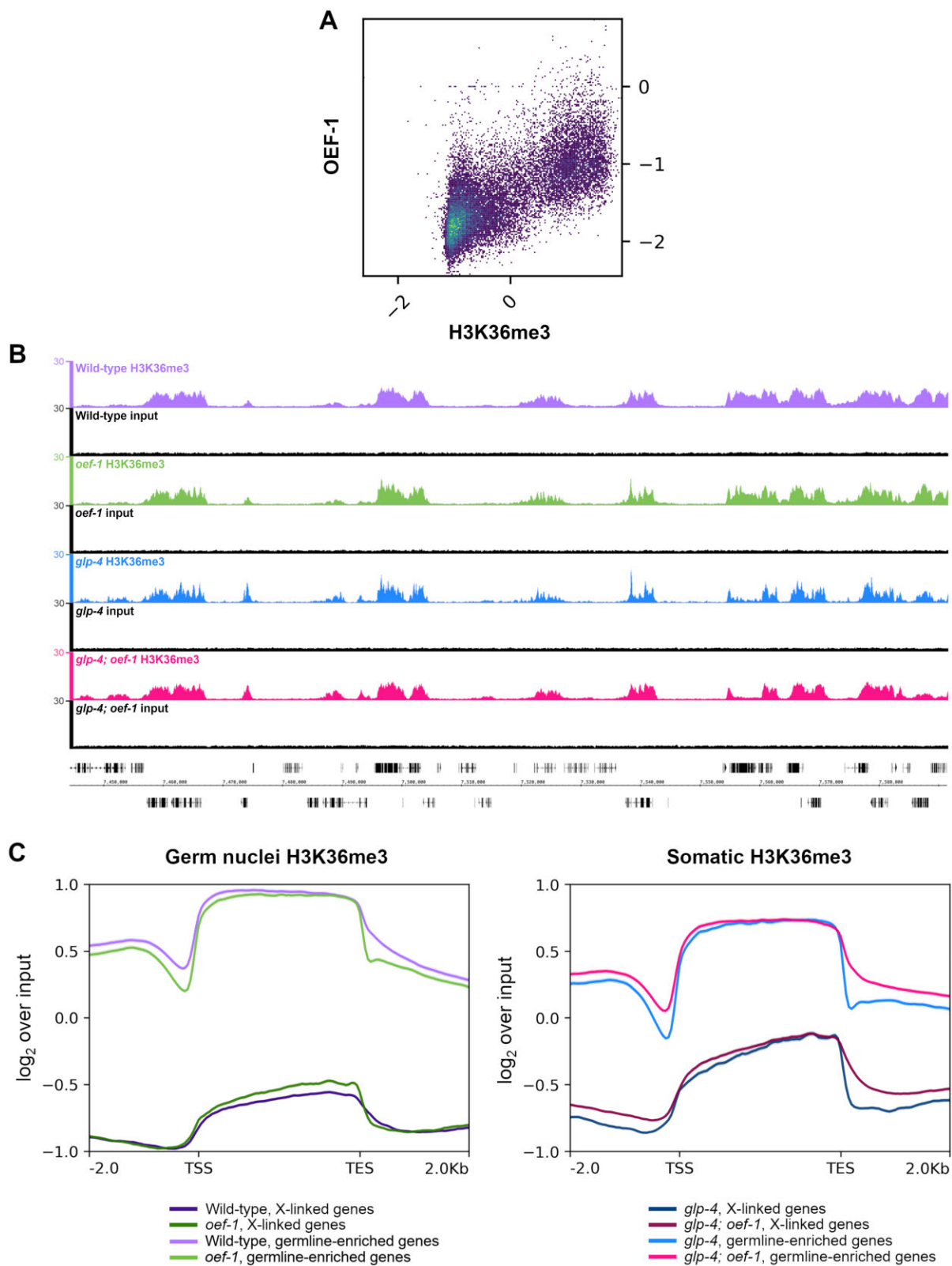


Figure 4 Loss of OEF-1 has minimal effect on H3K36me3 levels in germ nuclei. (A) Correlation plot comparing OEF-1 ChIP-seq signal (\log_2 over input) and wild-type germ nuclei H3K36me3 ChIP-seq (\log_2 over input) for all genes, including 2 kb up/downstream. Pearson's correlation coefficient = 0.70. (B) Screenshot of H3K36me3 ChIP-seq signal on chromosome I. Wild-type germ nuclei track is shown in purple, *oef-1* germ nuclei in green, *glp-4* soma in blue, *glp-4; oef-1* soma in pink. Input tracks in black are shown below each sample. Coordinates shown are chrI : 7,441,886–7,591,919. Scale bar, 10 kb. (C) Left: Metagenesis analysis of H3K36me3 ChIP-seq signal for wild-type (purple) and *oef-1* (*vr25*) (green) isolated germ nuclei across either X-linked genes (dark purple, dark green) or germline-enriched autosomal genes (light purple and light green). ChIP-seq signal is \log_2 over input. Right: Metagenesis analysis of H3K36me3 ChIP-seq signal for *glp-4* (blue) and *glp-4; oef-1* (pink) somatic samples across either X-linked genes (navy, dark pink) or germline-enriched autosomal genes (blue and pink). TSS, transcription start site. TES, transcription end site. Shading indicates standard error.

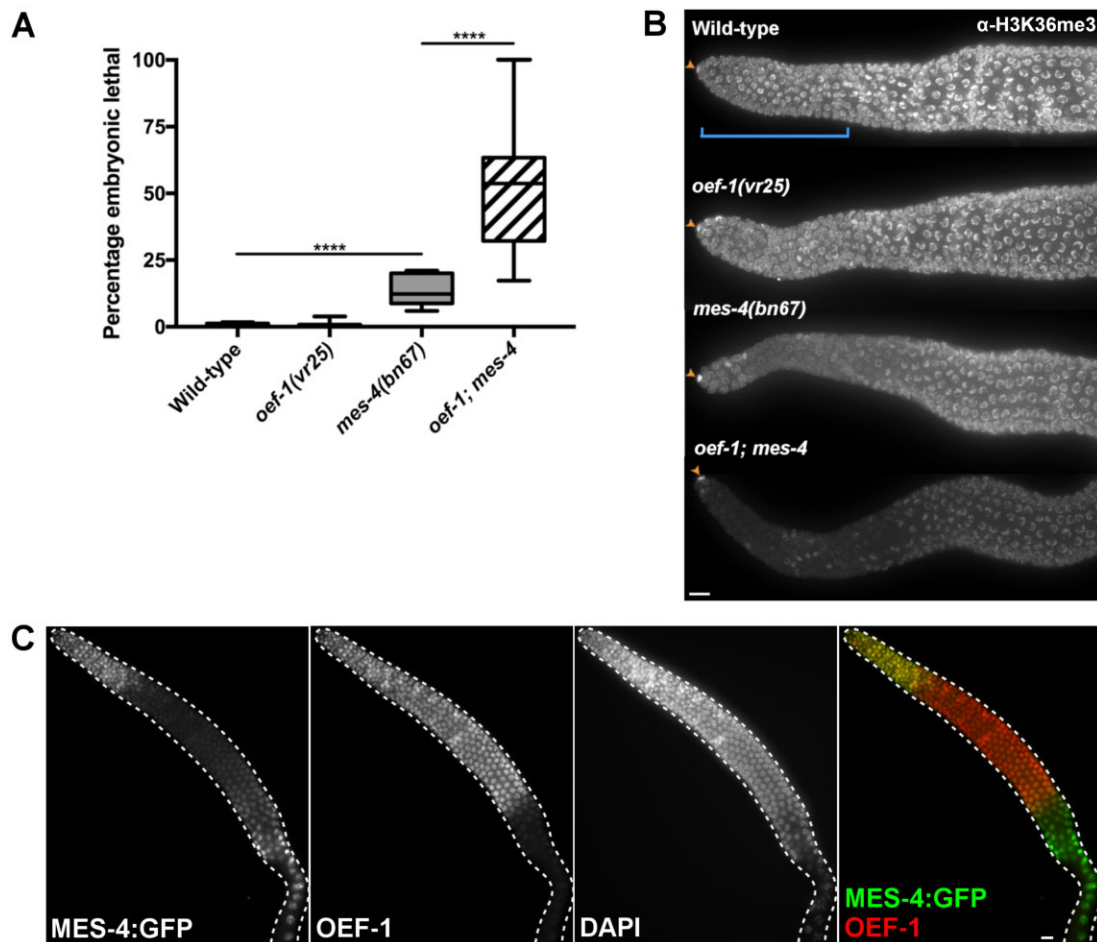


Figure 5 Loss of *oef-1* enhances *mes-4* phenotypes. (A) Quantification of embryonic lethality in *oef-1; mes-4* broods. *oef-1; mes-4* broods exhibit high levels of embryonic lethality relative to *mes-4* single mutants. **** $P \geq 0.0001$, unpaired t-test. $n \geq 10$ parental animals per genotype. Whiskers indicate min/max. (B) Representative Z projection images of H3K36me3-stained adult gonads. Proliferative zone is identified by DNA morphology (Francis et al. 1995) and is indicated by blue bracket in wild type. Orange arrows indicate the somatic distal tip cell, for which staining is unaffected between genotypes. Images were acquired under identical exposure times. Scale bar, 10 μ m. Quantification provided in Supplementary Figure S9A. (C) MES-4::GFP dissected adult gonad stained with GFP (green) and OEF-1 (red). MES-4::GFP levels reduce in the meiotic region before becoming detectable again in late pachytene as previously reported (Fong et al. 2002). OEF-1 levels decrease abruptly at late pachytene (McManus and Reinke 2018). Scale bar, 10 μ m.

might have a genetic interaction with the MES pathway, which establishes these two marks in germ cells. Specifically, because OEF-1 and MES-4 have opposite effects on X-linked H3K27me3, we expected that loss of OEF-1 might suppress the second-generation sterility of *mes* mutants (Capowski et al. 1991). To test this possibility, we created strains lacking *oef-1* as well as either *mes-4* (the HMT responsible for H3K36me3) (Bender et al. 2006) or *mes-2* (the catalytic subunit of PRC2 that deposits H3K27me3) (Bender et al. 2004). Contrary to expectation, loss of *oef-1* enhanced *mes* phenotypes. Embryonic lethality was elevated in the offspring of first-generation *oef-1; mes-4* double mutants relative to *mes-4* single mutants (Figure 5A, Supplementary Table S2) (51.6% vs 13.7%, $P < 0.0001$). Abnormal chromatin organization was frequently noted in the double mutant embryos, which might contribute to the lethality (Supplementary Figure S8). High levels of embryonic lethality also occurred when *oef-1* was crossed to a second *mes-4* allele (Supplementary Table S3). Consistent with the *mes-4* single mutant phenotype, *oef-1; mes-4* F2 survivors became sterile adults (Supplementary Table S4). In addition, *mes-2; oef-1* first-generation mutants showed a small but significant increase in embryonic lethality (5.55% vs 1.44% in *mes-2* single mutants, $P < 0.0001$) (Supplementary Table S5). *mes-*

2; oef-1 double mutants also exhibited an increase in the incidence of males (1.61% vs 0.42% in *mes-2* single mutants, $P < 0.0001$), suggesting higher rates of X chromosome nondisjunction. These results indicate that loss of OEF-1 has a greater effect in *mes-4* mutants relative to *mes-2* mutants, consistent with colocalization of OEF-1 and MES-4 at germline-expressed genes (Rechtsteiner et al. 2010; McManus and Reinke 2018).

We speculated that the strong genetic interaction between *oef-1* and *mes-4* might be due to synergistic effects on H3K36me3 levels, and therefore performed immunostaining of H3K36me3 (Figure 5B, Supplementary Figure S9). Consistent with the ChIP-seq data, *oef-1* mutant germlines displayed H3K36me3 levels similar to wild type. *mes-4* single mutants occasionally showed a decrease in H3K36me3 staining in the proliferative zone, as reported previously (Kreher et al. 2018). Strikingly, *oef-1; mes-4* double mutants exhibited even stronger reduction in H3K36me3 levels, particularly in the proliferative zone, where both OEF-1 and MES-4 are present at high levels (Figure 5C, Supplementary Figure S9A). Thus, loss of OEF-1 enhanced the reduction of H3K36me3 in *mes-4* mutants specifically in the region of the germline in which the two proteins colocalize, which might underlie the enhanced phenotypes seen in the *oef-1; mes-4*

mutant. We tested the specificity of this interaction by examining the relationship between OEF-1 and the only other H3K36me3 HMT in *C. elegans*, MET-1 (Kreher et al. 2018). *oef-1*; *met-1* double mutants did not display any significant alteration in H3K36me3 levels compared to either single mutant (Supplementary Figure S9B). Thus, *oef-1* specifically enhances *mes-4* but not *met-1* defects in H3K36me3 levels.

The relationship of *oef-1* with *mes-4* in maintaining H3K36me3 levels suggested that OEF-1 might function with other known H3K36me3-associated proteins. We therefore tested whether *oef-1* might also have a genetic interaction with *mrg-1*, the ortholog of another H3K36me3-associated protein, MRG15 (Iwamori et al. 2016). Strikingly, loss of *oef-1* also enhanced the *mrg-1* phenotype, leading to sterility one generation earlier than the *mrg-1* mutant alone (Supplementary Table S6). Thus, OEF-1 enhances the phenotypes of two factors associated with H3K36me3, reinforcing the possibility that OEF-1 acts at sites of H3K36me3 in germ cells and might influence H3K36me3-related processes.

Loss of OEF-1 activity decreases splicing efficiency in the germline

Of the downstream molecular processes associated with H3K36me3 that might be affected by OEF-1, we focused on mRNA splicing, since OEF-1 binds across both exons and introns. Using the RNA-seq data from dissected wild type and *oef-1* mutant gonads, we analyzed the frequency of intron retention, which indicates a disruption of normal splicing events. To rigorously define the baseline variation of intron retention that might normally occur between any two independent samples, we established a control comparison between our wild-type sample and an independently collected wild-type dataset, also from dissected gonads (Herbette et al. 2020) (Supplementary Figure S10). We then determined the rate of intron retention between *oef-1* and our wild-type sample and found that loss of OEF-1 activity led to significantly increased intron retention compared to this control (Figure 6A). Moreover, genes with increased intron retention in *oef-1* mutants exhibit properties consistent with OEF-1 localization: they are biased toward autosomes (Figure 6B) and have preferential expression in the germline (Figure 6C). These genes encode proteins associated with germline functions (Figure 6D), including several involved in the cell cycle, meiosis, and nuclear organization (e.g., *mcm-7*, *cdc-25.1*, *cya-1*, *cdc-42*, *nuc-1*, *sun-1*, *tac-1*, and *lmn-1*) that might underlie the precocious proliferation and increased apoptosis phenotypes seen upon loss of *oef-1*. Indeed, these candidate genes display OEF-1 binding (Supplementary Figure S11). By contrast, genes with more intron retention in the wild type control are biased toward genes expressed in the soma and encode proteins associated with zygotic functions. Finally, a negative correlation exists between transcript abundance and intron retention in *oef-1* mutants: genes with decreased transcript abundance are biased toward increased intron retention, whereas genes with increased transcript abundance are biased toward less intron retention (Figure 6E). This observation suggested that increased intron retention might lead to increased transcript degradation, and indeed we found that *oef-1* mutants displayed lower transcript integrity, a hallmark of RNA degradation (Figure 6F). Together these observations indicate that OEF-1 contributes to the efficient splicing of germline-expressed genes, perhaps via its association with H3K36me3.

Discussion

Here, we describe a potential molecular role for the germline-expressed zinc-finger protein OEF-1 and provide insight into how the pathways that balance H3K36me3 and H3K27me3 in the germline can be modulated. OEF-1 associates with genes with relatively higher levels of H3K36me3 but is not essential to maintain those levels. Thus, we propose that OEF-1 might act as a “reader” of H3K36me3 or associate with such a “reader” protein (Supplementary Figure S12). Different H3K36me3 reader protein complexes can affect cryptic transcription initiation, splicing, RNA processing, chromatin remodeling, and DNA repair (Li et al. 2019). Indeed, we find evidence that OEF-1 does affect splicing integrity of autosomal germline-expressed genes with higher levels of H3K36me3. Notably, the genes with increased intron retention in *oef-1* mutants display a mild decrease in gene expression (Figure 6F), which could be a consequence of degradation of the aberrant transcripts (Figure 6G). Presumably, the splicing defects and changes in degradation rates would occur variably among germline-expressed transcripts, which would explain why we identified relatively few autosomal genes with statistically significant changes in gene expression (Figure 1, A and B). In addition, other RNA processing defects that we did not assay might also occur in *oef-1* mutants and contribute to the variable transcript degradation (e.g., Meers et al. 2017).

Alteration of splicing patterns could contribute to the organismal phenotypes of precocious proliferation, faster germ cell progression, and defective synaptic checkpoint in *oef-1* mutants (McManus and Reinke 2018). Indeed, some genes with increased intron retention upon loss of OEF-1 encode proteins with cell cycle and meiotic functions. Whether OEF-1 interacts with various splicing regulators or other H3K36me3 reader proteins remains to be determined. For example, OEF-1 might associate with MRG-1, which also affects proliferation and the synaptic checkpoint in the germline (Takasaki et al. 2007; Dombecki et al. 2011), and indeed we found that loss of OEF-1 enhances *mrg-1* mutant sterility. In addition, even though OEF-1 associates with chromatin, it might do so indirectly through an interaction with nascent mRNA undergoing splicing. OEF-1 has a single C2H2 zinc finger domain, which might interact with either RNA or DNA, and an unstructured, possibly intrinsically disordered domain of about 80 amino acids at the C terminus, which might help in forming protein complexes. Systematic identification of OEF-1-interacting proteins will be essential for understanding how it reads or transmits the information from H3K36me3 patterns in the germline to affect downstream processes.

Based on our current genetic and molecular data, we suggest that OEF-1 might stabilize H3K36me3 levels, perhaps by limiting access by demethylases (Supplementary Figure S12). Decreased H3K36me3 is not detected in *oef-1* mutants as long as MES-4, the HMT that actively maintains pre-existing H3K36me3 patterns (Rechtsteiner et al. 2010), is present. However, the absence of both MES-4 and OEF-1 leads to a substantial decrease in H3K36me3 levels compared to the loss of either alone. In this model, we speculate that the absence of OEF-1 might cause elevated MES-4 activity to maintain normal levels of H3K36me3 at existing sites. MES-4 repels PRC2 activity, concentrating it to the X and other silenced genes (Gaydos et al. 2012). Thus, in *oef-1* mutants, increased MES-4 activity at its normal sites of action could indirectly result in increased H3K27me3 on the X and at “silenced” autosomal genes. The milder phenotype noted in *mes-2*; *oef-1* mutants relative to *oef-1*; *mes-4* mutants is consistent with this idea. *mes-2* mutants already lack detectable H3K27me3 in

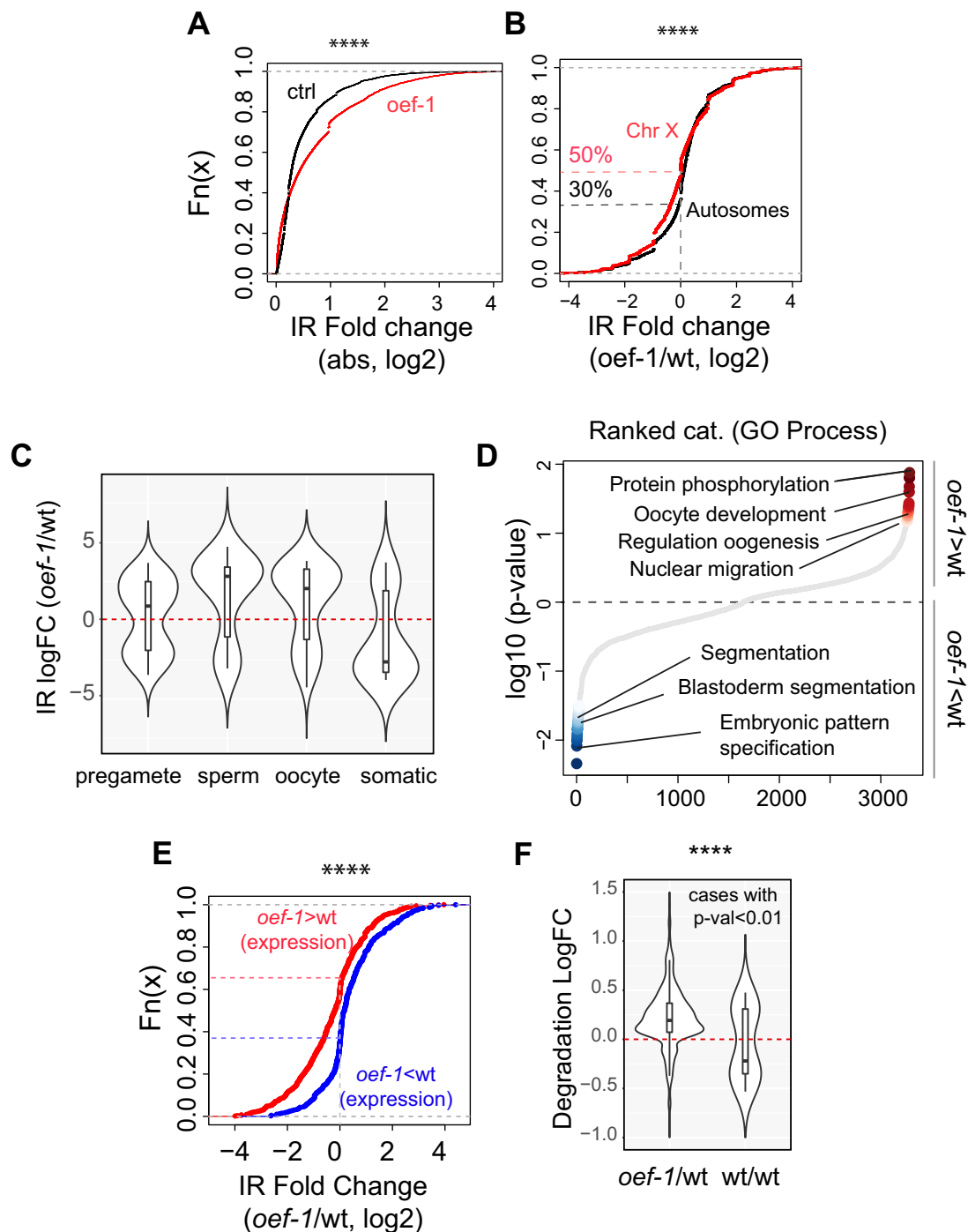


Figure 6 *oef-1* mutants exhibit decreased splicing integrity. (A) Cumulative plot showing an increase in intron retention in *oef-1* vs wild type (labeled *oef-1/wt*) relative to wild type vs an independent wild type sample (Herbette et al. 2020; labeled control, ctrl). Differential intron retention [IR, absolute log₂ fold change (FC)] is on the x-axis, and accumulated incidence (cumulative frequency) on the y-axis for the *oef-1/wt* (red) and control (black) comparisons. $P < 2.2 \times 10^{-16}$, Wilcoxon test. (B) Cumulative plot showing relative frequency of intron retention (IR) on autosomal introns compared to X-linked introns for the *oef-1/wt* dataset. The dotted lines mark log fold change = 0, showing that about 50% of X-linked genes (red) have increased intron retention in *oef-1* mutants relative to control, compared to 64% of autosomal genes (black). $P = 0.01$, Wilcoxon test. (C) Violin plots showing relative frequency of intron retention in *oef-1* mutants vs wild type for genes expressed in either immature germ cells (pregam) or differentiating germ cells (sperm, oocyte) or in the soma (Lee et al. 2017). (D) Graph of significant GO terms for genes with increased (red) or decreased (blue) intron retention in *oef-1* mutants vs wild type. (E) Cumulative plot showing relative frequency of intron retention for genes with either increased (red) or decreased (blue) expression in *oef-1* mutants relative to wild type (includes all genes with 0.5 log₂ fold change or greater, no significance cutoff). Dotted lines show percentage of the two distributions at log FC = 0. About 66% of genes with lower expression in *oef-1* mutants also have increased intron retention, compared to only 40% of genes with higher expression in *oef-1* mutants, $P < 2.2 \times 10^{-16}$, Wilcoxon test. (F) Violin plot showing significantly increased levels of transcript degradation in the experimental dataset relative to the control dataset, $P = 0.03$, Wilcoxon test; only cases with significant transcript degradation rate (measured with P-value < 0.01) are displayed.

germ nuclei (Bender *et al.* 2004), and as such the loci that typically have this modification would be minimally affected in *mes-2*; *oef-1* mutants. In this way, OEF-1 could influence the levels of histone modifying activity at both active and “silenced” genes in the germline. Future genomic studies will determine at high resolution how these competing histone marks are altered when the activity of both OEF-1 and the associated HMT complexes are simultaneously disrupted.

Data availability

The gene expression omnibus (GEO) accession number for the ChIP-seq and RNA-seq datasets reported in this paper is GSE147401. Previously published OEF-1::GFP ChIP-seq is available under accession number GSE107190 (McManus and Reinke 2018). Supplementary material is available at figshare: <https://doi.org/10.25387/g3.16586714>.

Acknowledgments

The authors would like to thank Dr. James Noonan for use of equipment and Mark Noble for construction of the *met-1*; *oef-1* strain. Some strains were provided by the *Caenorhabditis* Genetics Center (NIH P40 OD010440).

Funding

This work was supported by the K.S. and Feili Lo Foundation (Graduate Fellowship for Excellence in Stem Cell Research awarded to C.M.). This work was also supported by the National Institutes of Health (T32 GM007499 supported C.M.; R01 GM108663 and R35 GM131776 awarded to V.R. and supported M.M.).

Conflicts of interest

The authors declare that there is no conflict of interest.

Literature cited

- Anders S, Huber W. 2010. Differential expression analysis for sequence count data. *Genome Biol.* 11:R106.
- Beanan MJ, Strome S. 1992. Characterization of a germ-line proliferation mutation in *C. elegans*. *Development.* 116:755–766.
- Bender LB, Cao R, Zhang Y, Strome S. 2004. The MES-2/MES-3/MES-6 complex and regulation of histone H3 methylation in *C. elegans*. *Curr Biol.* 14:1639–1643.
- Bender LB, Suh J, Carroll CR, Fong Y, Fingerman IM, *et al.* 2006. MES-4: an autosome-associated histone methyltransferase that participates in silencing the X chromosomes in the *C. elegans* germline. *Development.* 133:3907–3917.
- Brenner S. 1974. The genetics of *Caenorhabditis elegans*. *Genetics.* 77: 71–94.
- Capowski EE, Martin P, Garvin C, Strome S. 1991. Identification of grandchildless loci whose products are required for normal germ-line development in the nematode *Caenorhabditis elegans*. *Genetics.* 129:1061–1072.
- Dombecki CR, Chiang AC, Kang HJ, Bilgir C, Stefanski NA, *et al.* 2011. The chromodomain protein MRG-1 facilitates SC-independent homologous pairing during meiosis in *Caenorhabditis elegans*. *Dev Cell.* 21:1092–1103.
- Evans KJ, Huang N, Stempor P, Chesney MA, Down TA, *et al.* 2016. Stable *Caenorhabditis elegans* chromatin domains separate broadly expressed and developmentally regulated genes. *Proc Natl Acad Sci USA.* 113:E7020–E7029.
- Fong Y, Bender L, Wang W, Strome S. 2002. Regulation of the different chromatin states of autosomes and X chromosomes in the germ line of *C. elegans*. *Science.* 296:2235–2238.
- Francis R, Barton MK, Kimble J, Schedl T. 1995. *gld-1*, a tumor suppressor gene required for oocyte development in *Caenorhabditis elegans*. *Genetics.* 139:579–606.
- Gaydos LJ, Rechtsteiner A, Egelhofer TA, Carroll CR, Strome S. 2012. Antagonism between MES-4 and Polycomb repressive complex 2 promotes appropriate gene expression in *C. elegans* germ cells. *Cell Rep.* 2:1169–1177.
- Gene Ontology Consortium. 2021. The Gene Ontology resource: enriching a GOLD mine. *Nucleic Acids Res.* 49:D325–D334.
- Han M, Wei G, McManus CE, Hillier LW, Reinke V. 2019. Isolated *C. elegans* germ nuclei exhibit distinct genomic profiles of histone modification and gene expression. *BMC Genomics.* 20:500.
- Herbette M, Robert V, Bailly A, Gely L, Feil R, *et al.* 2020. A role for *Caenorhabditis elegans* COMPASS in germline chromatin organization. *Cells.* 9:2049.
- Iwamori N, Tominaga K, Sato T, Riehle K, Iwamori T, *et al.* 2016. MRG15 is required for pre-mRNA splicing and spermatogenesis. *Proc Natl Acad Sci USA.* 113:E5408–E5415.
- Kelly WG, Schaner CE, Dernburg AF, Lee MH, Kim SK, *et al.* 2002. X-chromosome silencing in the germline of *C. elegans*. *Development.* 129:479–492.
- Kim D, Paggi JM, Park C, Bennett C, Salzberg SL. 2019. Graph-based genome alignment and genotyping with HISAT2 and HISAT-genotype. *Nat Biotechnol.* 37:907–915.
- Kim D, Pertea G, Trapnell C, Pimentel H, Kelley R, *et al.* 2013. TopHat2: accurate alignment of transcriptomes in the presence of insertions, deletions and gene fusions. *Genome Biol.* 14:R36.
- Kreher J, Takasaki T, Cockrum C, Sidoli S, Garcia BA, *et al.* 2018. Distinct roles of two histone methyltransferases in transmitting H3K36me3-based epigenetic memory across generations in *Caenorhabditis elegans*. *Genetics.* 210:969–982.
- Kudron MM, Victorsen A, Gevirtzman L, Hillier LW, Fisher WW, *et al.* 2018. The ModERN Resource: genome-wide binding profiles for hundreds of *Drosophila* and *Caenorhabditis elegans* transcription factors. *Genetics.* 208:937–949.
- Langmead B, Salzberg SL. 2012. Fast gapped-read alignment with Bowtie 2. *Nat Methods.* 9:357–359.
- Lee CS, Lu T, Seydoux G. 2017. Nanos promotes epigenetic reprogramming of the germline by down-regulation of the THAP transcription factor LIN-15B. *Elife.* 6:e30201.
- Li H, Handsaker B, Wysoker A, Fennell T, Ruan J, *et al.*; 1000 Genome Project Data Processing Subgroup. 2009. The Sequence Alignment/Map format and SAMtools. *Bioinformatics.* 25: 2078–2079.
- Li J, Ahn JH, Wang GG. 2019. Understanding histone H3 lysine 36 methylation and its deregulation in disease. *Cell Mol Life Sci.* 76: 2899–2916.
- Liao Y, Smyth GK, Shi W. 2019. The R package Rsubread is easier, faster, cheaper and better for alignment and quantification of RNA sequencing reads. *Nucleic Acids Res.* 47:e47.
- Love MI, Huber W, Anders S. 2014. Moderated estimation of fold change and dispersion for RNA-seq data with DESeq2. *Genome Biol.* 15:550.
- Luo W, Friedman MS, Shedden K, Hankenson KD, Woolf PJ. 2009. GAGE: generally applicable gene set enrichment for pathway analysis. *BMC Bioinformatics.* 10:161.

- McManus CE, Reinke V. 2018. The germline-specific factor OEF-1 facilitates coordinated progression through germ cell development in *C. elegans*. *Genetics*. 208:549–563.
- Meers MP, Henriques T, Lavender CA, McKay DJ, Strahl BD, et al. 2017. Histone gene replacement reveals a post-transcriptional role for H3K36 in maintaining metazoan transcriptome fidelity. *Elife*. 6:e23249.
- Oghabian A, Greco D, Frilander MJ. 2018. IntERESt: intron-exon retention estimator. *BMC Bioinformatics*. 19:130.
- Ortiz MA, Noble D, Sorokin EP, Kimble J. 2014. A new dataset of spermatogenic vs. oogenic transcriptomes in the nematode *Caenorhabditis elegans*. *G3 (Bethesda)*. 4:1765–1772.
- Ramírez F, Ryan DP, Gruning B, Bhardwaj V, Kilpert F, et al. 2016. deepTools2: a next generation web server for deep-sequencing data analysis. *Nucleic Acids Res*. 44:W160–W165.
- Rechtsteiner A, Ercan S, Takasaki T, Phippen TM, Egelhofer TA, et al. 2010. The histone H3K36 methyltransferase MES-4 acts epigenetically to transmit the memory of germline gene expression to progeny. *PLoS Genet*. 6:e1001091.
- Reinke V, Gil IS, Ward S, Kazmer S. 2004. Genome-wide germline-enriched and sex-biased expression profiles in *C. elegans*. *Development*. 131:311–323.
- Shen L, Shao N, Liu X, Nestler E. 2014. ngs.plot: Quick mining and visualization of next-generation sequencing data by integrating genomic databases. *BMC Genomics*. 15:284.
- Takasaki T, Liu Z, Habara Y, Nishiwaki K, Nakayama J, et al. 2007. MRG-1, an autosome-associated protein, silences X-linked genes and protects germline immortality in *Caenorhabditis elegans*. *Development*. 134:757–767.
- Trapnell C, Hendrickson DG, Sauvageau M, Goff L, Rinn JL, et al. 2013. Differential analysis of gene regulation at transcript resolution with RNA-seq. *Nat Biotechnol*. 31:46–53.
- Trapnell C, Roberts A, Goff L, Pertea G, Kim D, et al. 2012. Differential gene and transcript expression analysis of RNA-seq experiments with TopHat and Cufflinks. *Nat Protoc*. 7:562–578.
- Trapnell C, Williams BA, Pertea G, Mortazavi A, Kwan G, et al. 2010. Transcript assembly and quantification by RNA-Seq reveals unannotated transcripts and isoform switching during cell differentiation. *Nat Biotechnol*. 28:511–515.
- van Mierlo G, Veenstra GJC, Vermeulen M, Marks H. 2019. The complexity of PRC2 subcomplexes. *Trends Cell Biol*. 29:660–671.
- Wang L, Nie J, Sicotte H, Li Y, Eckel-Passow JE, et al. 2016. Measure transcript integrity using RNA-seq data. *BMC Bioinformatics*. 17:58.
- Wickham H. 2016. ggplot2: Elegant Graphics for Data Analysis. New York: Springer-Verlag. ISBN 978-3-319-24277-4.
- Zhang Y, Liu T, Meyer CA, Eeckhoute J, Johnson DS, et al. 2008. Model-based analysis of ChIP-Seq (MACS). *Genome Biol*. 9:R137.

Communicating editor: D. Fay